Spatiotemporal transcriptomics reveals pathogenesis of viral myocarditis

Authors: Madhav Mantri[1], Meleana M. Hinchman[2], David W. McKellar[1], Michael F. Z. Wang[1], Shaun T. Cross[1,2,3], John S. L. Parker[2,3*], Iwijn De Vlaminck[1,3*]

Affiliations: [1]Nancy E. and Peter C. Meinig School of Biomedical Engineering, Cornell University, Ithaca, New York, [2]Baker Institute for Animal Health, College of Veterinary Medicine, Cornell University, Ithaca, New York, [3]Cornell Institute for Host-Microbe Interactions and Disease, Cornell University, Ithaca, New York.

*To whom correspondence should be addressed: vlaminck@cornell.edu and jsp7@cornell.edu

ABSTRACT

A significant fraction of sudden death in children and young adults is due to myocarditis, an inflammatory disease of the heart, most often caused by viral infection. Here we used integrated single-cell and spatial transcriptomics to create a high-resolution, spatially resolved map of reovirus-induced myocarditis in neonatal murine hearts. We assayed hearts collected at three timepoints after reovirus infection and studied the temporal, spatial, and cellular heterogeneity of host-virus interactions. We further assayed the intestine, the primary site of reovirus infection to establish a full chronology of molecular events that ultimately lead to myocarditis. We implemented targeted enrichment of viral transcripts to establish the cellular targets of the virus in the intestine and the heart. Our data give insight into the cell-type specificity of innate immune responses, and into the transcriptional states of inflamed cardiac cells that recruit circulating immune cells, including cytotoxic T cells which induce pyroptosis in the myocarditic tissue. Analyses of spatially restricted gene expression in myocarditic regions and the border zone around those regions identified immune-mediated cell-type specific injury and stress responses. Overall, we observe a dynamic and complex network of cellular phenotypes and cell-cell interactions associated with viral myocarditis.

INTRODUCTION

Viral infection is the most common cause of myocarditis[1,2]. The resulting inflammatory cardiomyopathy can lead to arrhythmias, dilated cardiomyopathy, and death[1,3,4]. In humans, viral myocarditis is challenging to study because of the low sensitivity of available diagnostic testing, the acute onset of the disease, the focal nature of the disease, and the extreme heterogeneity of immune-virus interactions in complex cardiac tissues[4–6]. In mice, mammalian orthoreovirus offers a flexible model system[7]. After oral inoculation, the Type 1 Lang (T1L) reovirus strain initially infects the gastrointestinal tract. Within days the infection then spreads to secondary sites in the body, including the heart, leading to myocarditis in up to 50% of infections[7–9]. Yet, even in this mouse model, the molecular pathogenesis of viral myocarditis is difficult to study because of the complex network of cardiac and immune cell types involved and the cellular, spatial, and temporal heterogeneity of the disease[2,10]. Consequently, neither the cell types that are responsible for the innate immune response, nor the cell types that are infected *in vivo* have been identified. Similarly, the responses of infected and uninfected bystander cells within the heart have not been characterized. In addition, the protective versus damaging effects of adaptive immune responses have not been quantified. Experiments in mice with severe combined immunodeficiency (SCID) indicate that adaptive immune responses are not required for myocardial injury and heart failure[7,11], but these observations do not exclude the possibility that immune-cell-mediated injury is important in immunocompetent mice. Unbiased characterization of all cellular phenotypes as a function of time and location within infected cardiac tissues is needed to address these knowledge gaps.

Here we used integrated single-cell and spatially resolved RNA-sequencing (RNA-seq) to study the cellular and spatial heterogeneity of myocarditic processes in the hearts of reovirus-infected neonatal mice at multiple time points after infection. We also applied these technologies to study the innate response to reovirus infection in the intestine. In addition, we performed time-series single-cell RNA-seq (scRNA-seq) of cardiac tissues of mice infected with a reovirus point mutant that does not cause myocarditis. To establish viral tropism, we implemented molecular enrichment of non-polyadenylated viral transcripts that were otherwise poorly represented in the transcriptomes. Our measurements give insight into the cell-type specificity of innate immune responses, into the tropism of the virus in the intestine and the heart, and into the transcriptional states of cell types involved in the production of inflammatory cytokines and the recruitment of circulating immune cells. Analyses of spatially restricted gene expression in myocarditic regions and the border zone around those regions identified injury and stress responses in different cell types, including cardiomyocytes. Overall, our data identify spatially restricted cellular interactions and cell-type specific host responses during reovirus-induced myocarditis.

2

65

RESULTS

Single-cell and spatial transcriptomics of reovirus T1L-infected neonatal mice hearts

To elucidate the pathogenesis of reovirus-induced myocarditis, we analyzed heart tissues collected from neonatal mice infected orally with either the T1L strain of reovirus or a mock control (**Methods, Fig. 1A**). We generated scRNA-seq data for 31,684 cells from infected hearts and mock controls at 4, 7, and 10 days post-infection (dpi), and 8,243 spatial transcriptomes for four tissue sections from infected hearts and mock controls at 4 and 7 dpi from the same litter (10x Chromium and 10x Visium, **Methods, Supp Fig. 1A-1B and Fig. 1B-1C**). The single-cell transcriptomes represented 18 distinct cell types, including cardiomyocytes, endocardial cells, cardiac fibroblasts, endothelial cells, mural cells, macrophages, neutrophils, NK cells, dendritic cells, T cells, and B cells (**Methods, Fig 1B, Supp Data 1, Supp Fig. 1C-F**). Clustering of the spatial transcriptomic data revealed distinct transcriptional programs for myocarditic regions and the border zone surrounding the myocarditic regions in the 7 dpi reovirus-infected heart that corresponded to areas of tissue damage identified by H&E staining (**Fig. 1C, Supp Fig. 2A-B**). The combination of scRNA-seq and spatial transcriptomics allowed us to resolve and visualize cell types and gene expression in a spatial context (**Supp Fig. 2C**). Because the virus first infects the gastrointestinal tract before it spreads to other body sites including the heart, we also performed scRNA-seq and spatial transcriptomics on ileum. We obtained 7,695 single-cell transcriptomes and 8,027 spatial spot transcriptomes for ileum from mock and infected samples at 1 and 4 dpi (**Fig. 1D, Supp Fig. 3A-D**).

To faithfully identify reovirus transcripts in the ileum and heart, which are not polyadenylated, we performed hybridization-based enrichment of viral fragments captured in the scRNA-seq libraries (**Methods, Supp Fig. 4A-C**). In the ileum, we captured a total of 13,100 unique viral transcripts, with viral load decreasing from 1 dpi to 4 dpi. At 1 dpi, entero-endocrine cells had the highest fraction of infected cells followed by enterocytes and goblet cells, all of which are present in the gut epithelium. Lymphatic endothelial cells were infected at 4 dpi, suggesting that the virus reaches the bloodstream via lymphatic drainage to allow transmission of the virus to secondary sites in the body, including the heart, as shown before[12] (**Supp Fig. 4D, Fig 1E**). We captured 2,762 unique viral transcripts from 392 cells in the T1L-infected hearts. The viral load first increased from 4 dpi to 7 dpi and then decreased from 7 dpi to 10 dpi, consistent with viral titer assays performed on whole hearts[9,13] (**Fig. 1E, Supp Fig. 4E**). Endocardial and endothelial cells were the most frequently infected cell types at 4 dpi, suggesting that endocardial cells lining the ventricular lumen and endothelial cells lining the cardiac vasculature are among the first cells to be infected (**Fig. 1E**). We detected an increased infection in endothelial cells from 4 dpi to 7 dpi, consistent with viral titer assays performed on whole hearts[9,13] (**Fig. 1E, Supp Fig. 4E**). We further detected viral transcripts in neutrophils, dendritic cells, and T cells in the 7 dpi heart (**Fig. 1E, Supp Fig. 4E)**. This observation

3

104 suggests that antigen-presenting cells and immune cells may contribute to the spread of
105 infection to other organs in the body. The role of infected dendritic cells in bringing more
106 reovirus to the cardiac tissue during systemic infection has been discussed previously[8].

107 To validate these observations, we performed histology, multiplexed RNA fluorescence in-situ
108 hybridization (FISH), and immunofluorescence assays on tissue sections from myocarditic
109 hearts and controls (multiple infected mice litters, **Supp Fig. 5A-5B, Methods**). We used RNA-
110 FISH to visualize expression of genes specific to cardiomyocytes, fibroblasts, endothelial cells,
111 macrophages, neutrophils, and T cells (**Supp Fig. 5C & 5E, Methods**). On consecutive tissue
112 sections, we labeled reovirus antigen using immunofluorescence to identify reovirus infected
113 cells (**Supp Fig. 5C**). These experiments revealed infection foci and immune infiltration in
114 myocarditic regions. We found macrophages and neutrophils in the border zones and outside
115 the myocarditic regions at 7 dpi (**Supp Fig. 5C, 5D**). In contrast, most T cells were found inside
116 the myocarditic regions at 7 dpi **(Supp Fig. 5D)**. Endothelial cells that were positive for the
117 reovirus antigen colocalized with T cells in the myocarditic regions. A small number of
118 fibroblasts were often located on the edges of these regions. Collectively, these results
119 indicate that vascular endothelial cells are targets of reovirus in the heart.
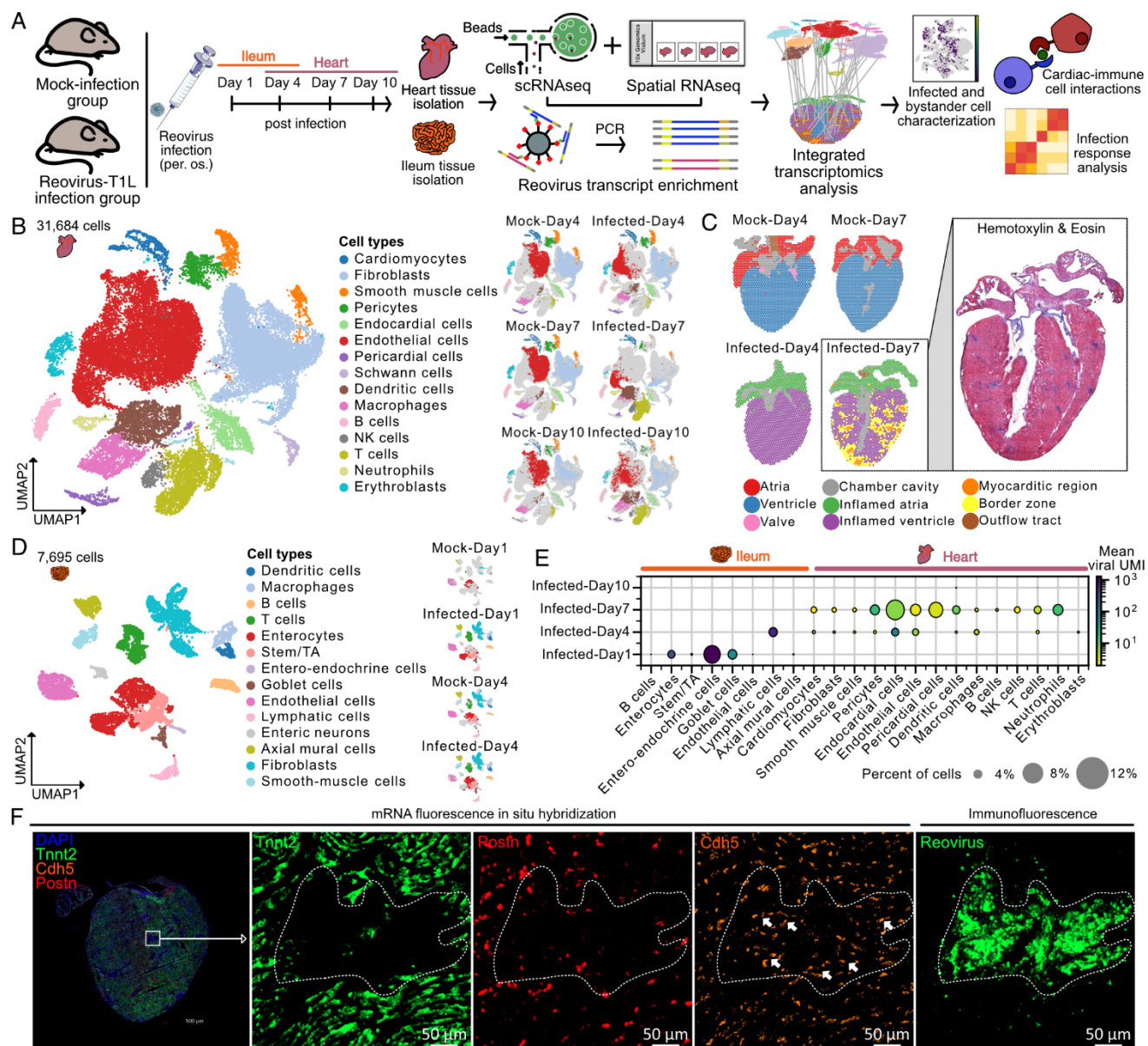
Figure 1: Single-cell and spatial transcriptomics of cardiac and ileum tissue of reovirus-infected neonatal mice. A) Experiment and analysis workflow. **B)** UMAP plot of 31,684 single-cell transcriptomes from mock-infected and reovirus-infected hearts at 4, 7, and 10 dpi, clustered by gene expression and colored by cell type (left). UMAP plots showing the gaussian kernel density of cells across samples for the heart scRNA-seq data (right). **C)** 8,243 spatial transcriptomes of cardiac tissue sections from mock-infected and reovirus-infected mice at 4 and 7 dpi. Hematoxylin and Eosin (H&E) stained image of reovirus-infected myocarditic tissue section used for spatial transcriptomics at 7 dpi (in box). **D)** UMAP plot of 7,695 single-cell transcriptomes from mock-infected and reovirus-infected ileum at day 1 and 4 dpi, clustered and colored by cell type (left). UMAP plots showing the gaussian kernel density of cells across samples for the ileum scRNA-seq data (right). **E)** Dot plot showing the percent of cells with non-zero viral transcripts and the mean viral transcript counts (UMIs) in ileal and cardiac cell types. **F)** Representative heart images showing mRNA FISH labelling of cardiac cell type markers (*Tnnt2* for cardiomyocytes, *Postn* for fibroblasts, and *Cdh5* for endothelial cells), and immunofluorescence staining of reovirus antigen showing reovirus-infected endothelial cells at 7 dpi.

Endothelial cells are primed with a basal interferon response and play an important role in initiating host innate immune responses

To detect early transcriptional differences in the cardiac tissue after infection, we performed Differential Gene Expression Analysis (DGEA, mock vs infected hearts at 4 dpi, **Methods**). This analysis revealed a significant upregulation of 226 genes in the infected heart (two-sided Wilcoxon test, log fold-change > 1.0 and p-value < 0.01), including genes related to the interferon-β pathway, interferon signaling, and innate immune responses (**Supp Fig 6A-6B, Fig. 2A**).

To quantify and compare the overall magnitude of early infection responses across different cell types, we computed a gene module score (infection response score, IR, module of 226 genes selected above). Comparison of the IR of different cell types in the absence of infection revealed a small, but higher IR in endothelial cells as compared to other cardiac cell types (**Fig. 2B**). In response to infection, an increase in IR was observed for all cardiac cell types, but the greatest increase in IR was observed for endothelial cells (**Fig. 2B**). These data suggest that endothelial cells lining the cardiac vasculature are important initiators of the host defense to viral infection. Comparison of IR scores using the spatial transcriptomic data showed increased IR scores in the infected hearts at 4 and 7 dpi with the highest scores found in myocarditic regions (**Fig. 2C**). Given our observation that endothelial cells within the heart had the highest IR score in the absence of infection, we asked if this observation was unique to heart tissue or was a more general phenomenon. To this end, we used the Tabula Muris scRNA-seq mouse atlas[14] and estimated the IR of ~16,000 cells of five major cell types (epithelial cells, fibroblasts, endothelial cells, smooth muscle cells, and mesenchymal cells) across 10 different organs and tissues. This analysis revealed that endothelial cells consistently had the highest IR score across all tissues in mice (**Fig. 2D**). These results indicate that endothelial cells lining the vasculature have a higher basal expression of innate response genes within most tissues, which may prime these cells to respond to viral dissemination within the blood and lymphatics.

To investigate the cell-type-specific IR in the ileum, the primary site of reovirus infection, we performed DGEA on reovirus-infected and mock-infected ileal cells at 1 dpi and found a significant upregulation of 438 genes (two-sided Wilcoxon test, log fold-change > 1.0 and p-value < 0.01), related to the interferon-beta pathway, interferon signaling, and innate immune responses in reovirus-infected ileal cells (**Supp Fig. 6C-6D**). We computed an IR score using this module of 438 genes and observed higher basal IR scores in enterocytes and entero-endocrine cells as compared to other ileal cell types (**Fig. 2E**). Enterocytes further showed the highest increase in IR score after infection, followed by entero-endocrine, endothelial, and lymphatic cells (**Fig. 2E**). Comparison of IR scores for spatial transcriptomic data further supported our analysis of the scRNA-seq data, showing increased IR scores in the infected ileum at 1 and 4 dpi with the highest scores evident within intestinal mucosa and villi (**Fig. 2F**). The intestinal epithelial cells must tolerate commensal microorganisms present in the lumen of the gut and yet still be responsive to invasive pathogens. Our data suggest that to achieve this,

6

175 enterocytes and entero-endocrine cells in the gut epithelium are primed with a basal interferon
176 response and play an important part in mounting innate immune responses in the early stages
177 of viral infection.

178
179 **Figure 2: Endothelial cells have the highest basal interferon response and the highest increase in innate**
180 **response upon reovirus infection A)** Heatmap showing the expression of the 25 most upregulated genes in the
181 reovirus-infected heart as compared to mock at 4 dpi. **B)** Infection response score for cardiac cell types in scRNA-
182 seq data across mock-infected and reovirus-infected hearts at three distinct stages. The infection response score
183 represents the gene module score for a panel of 226 genes that are significantly upregulated (two-sided Wilcoxon
184 test, log fold-change > 1.0 and p-value < 0.01) in the reovirus-infected heart as compared to the mock-infected
185 heart at 4 dpi. **C)** Infection response score (defined above) across spots in spatial transcriptomics data. **D)**
186 Infection response score calculated for five common cell types across 13 tissues from the tabula-muris mouse
187 atlas data. **E)** Infection response score for ileal cell types in scRNA-seq data across mock-infected and reovirus-
188 infected ileum at two distinct stages. The infection response score represents the gene module score for a panel
189 of 438 genes significantly upregulated (two-sided Wilcoxon test, log fold-change > 1.0 and p-value < 0.01) in the
190 reovirus-infected ileum at 1 dpi as compared to the mock-infected ileum. **F)** Infection response score for spatial
191 transcriptomics data from mock-infected and reovirus-infected ileum at two distinct stages.

192 **Cytotoxic T cells recruited by inflamed endothelial cells induce pyroptosis**

193 To explore the heterogeneity of endothelial cell phenotypes in more detail, we reclustered all
194 9,786 cardiac endothelial cells in the scRNA-seq data. We observed four distinct phenotypes:
195 *i)* uninflamed venous endothelial cells expressing *Nr2f2* and *Aplnr* mainly derived from the
196 mock controls[15], *ii)* arterial endothelial cells expressing *Gja4*, *Gja5*, and *Cxcl12* derived from
197 both mock and infected cardiac hearts[15], *iii)* inflamed endothelial cells derived from infected

7

198 hearts at 4 and 10 dpi, and *iv)* inflamed endothelial cells from the heart at 7 dpi, with both
199 inflamed endothelial cell clusters expressing *Isg15*, *Iigp1*, and *Ly6a* (**Fig. 3A-B**). DGEA across
200 endothelial subclusters revealed that the inflamed 7 dpi endothelial cells overexpressed
201 chemokines *Cxcl9* and *Cxcl10*, which are generally involved in immunoregulatory and
202 inflammatory processes, but more specifically in the recruitment of T cells and NK T cells[16]
203 (**Fig. 3B-3C, Supp Fig. 7A**). In line with this observation, T cells in the 7 dpi hearts expressed
204 the *Cxcr3* receptor (see below). The *Cxcl9*-high inflamed endothelial cells furthermore
205 expressed high levels of cell adhesion marker genes *Vcam1* and *Icam1*, which help immune
206 cells in the blood to attach to endothelial cells[17] (**Fig. 3C, Supp Fig. 7A, 7E**). The endothelial
207 cells also overexpressed MHC class 1 (*H2-D1* and *H2-K1*) and MHC class 2 (*Cd74*)
208 molecules, suggesting their involvement in antigen presentation to adaptive immune cells (**Fig.
209 3B-C, Supp Fig. 7A, 7E)**. Endothelial cells have been shown to be involved in antigen
210 presentation and shaping the cellular immune response in infectious myocarditis[17,18]. Gene
211 ontology (GO) term enrichment analysis identified pathways further supporting the *Cxcl9*-high
212 endothelial cells' involvement in leukocyte cell-cell adhesion, T cell activation, regulation of
213 interleukin-8 production, and response to cytokines, interferon-gamma, interleukin-1, and
214 tumor necrosis factors (**Supp Fig. 7B**).

215 The observation that endothelial cells are involved in the recruitment of T cells prompted us to
216 explore the heterogeneity of T cells in the infected hearts in more detail. To this end, we
217 reclustered 2,205 T cell single-cell transcriptomes, leading to four subclusters representing
218 three T cell subtypes, *i)* *Cd8*+ cytotoxic T cells, *ii)* *Cd4*+ helper T cells, and *iii)* naive T cells
219 (**Fig 3E-F**). Both the cytotoxic and helper T cells identified within infected hearts expressed
220 *Cxcr3* receptor, interferon-gamma (*Ifng),* and the chemokines *Ccl3, Ccl4, Ccl5, S100A4,* and
221 *S100A6,* suggesting their involvement in neutrophil recruitment and activation (**Fig. 3G**, **Supp
222 Fig. 7C**). The *Cxcr3* receptor binds selectively to the chemokines *Cxcl9* and *Cxcl10*, promoting
223 chemotaxis (**Fig. 3G**). Cytotoxic T cells represented the majority of infiltrating T cells and
224 expressed *Prf1*, *Gzma*, *Gzmb*, and *Gzmk,* coding for lytic molecules associated with the
225 granzyme-dependent exocytosis pathway[19] (**Fig. 3F-G, Supp Fig. 7C, 7G**). These cells also
226 expressed tumor necrosis factor superfamily genes *Fasl* and *Tradd*, which are involved in the
227 Fas-induced cell death pathway. *Fasl* binds to *Fas* on the surface of target cells and mediates
228 programmed cell death signaling and NF-κB activation (**Fig. 3G**). The Fasl-Fas apoptosis
229 pathway is important in regulating T cells, in promoting tolerance to self-antigens, and is a
230 mechanism by which cytotoxic T cells kill target cells[19]. GO term enrichment analysis identified
231 pathways involved in neutrophil activation and degranulation, processing and presentation of
232 exogenous peptide antigen, interleukin-1-mediated signaling pathway, tumor necrosis factor-
233 mediated signaling, NF-κB-inducing kinase (NIK) /NF-κB signaling, cellular response to
234 hypoxia, and apoptotic processes (**Supp Fig. 7D**).

235 The downstream gene markers for cell death-associated pathways *Pycard*, *Acer2, Zbp1,* and
236 Caspases *Casp1*, *Casp4*, and *Casp12* were enriched in the *Cxcl9*-high endothelial cells. This
237 raises the possibility that cytotoxic lymphocytes are responsible for inflamed endothelial cell

8

238 death (**Fig. 3B-3C, Supp Fig. 7E**). GO term enrichment of endothelial cells confirmed an
239 upregulation of cell death pathways including activation of cysteine-type endopeptidase activity
240 involved in the apoptotic process, positive regulation of the extrinsic apoptotic signaling
241 pathway, and pyroptosis pathway (**Supp Fig. 7B**). We assessed the spatial transcriptomic data
242 to validate direct interactions between *Cxcl9*-high inflamed endothelial cells and T cells and
243 found that they were indeed spatially co-localized in the myocarditic regions and the border
244 zone (**Supp Fig. 2C**). We calculated gene module scores for genes associated with ontology
245 terms enriched in *Cxcl9*-high endothelial and cytotoxic T cells for spatial transcriptomics data
246 and found these pathways to be enriched in the myocarditic regions (**Fig. 3D, 3H,** and **Supp**
247 **Fig. 7E-H**).

248 We used histology, multiplexed RNA fluorescence in-situ hybridization (FISH), and
249 immunofluorescence to validate our spatial transcriptomic and scRNA-seq findings on matched
250 tissue sections from myocarditic and mock-infected hearts. (**Supp Fig. 8A, 8B, Methods**). The
251 RNA FISH experiments confirmed the presence of Cxcl9-high endothelial cells (detected with
252 *Cdh5*) within myocarditic tissue with infiltrating T cells marked by expression of Trbc*2*, *Cxcr3*,
253 and lytic molecule *Prf1* (**Supp Fig. 8B, Fig. 3I**). We also detected expression of the pyroptosis-
254 mediated cell death marker *Casp1* within endothelial cells supporting our hypothesis that T
255 cell-induced pyroptosis in endothelial cells occurs within myocarditic tissue **(Supp Fig. 8B, Fig.**
256 **3I)**. Most of the T cells in the myocarditic tissue expressed the *Prf1* marker for cytotoxic T cells
257 and these cells were often observed in proximity of endothelial cells expressing *Casp1* mRNA.
258 We used immunofluorescence to detect Casp1 protein in endothelial cells within myocarditic
259 tissue on a consecutive tissue section **(Supp Fig. 8C, Fig. 3J)**. We further labeled Casp1
260 protein and stained calcium deposits using Alizarin Red on independent serial sections from
261 myocarditic hearts and found Casp1+ myocarditic regions to be the sites of calcification in the
262 infected tissue at 7 dpi (**Supp Fig. 8D**).

263 Collectively, these results suggest that endothelial cells lining the cardiac vasculature act as a
264 blood-heart barrier and play an important role in the recruitment and activation of the host
265 adaptive immune system. These cells may be the target of both direct viral damage and
266 immune-mediated damage during reovirus-induced myocarditis. Damage to the
267 microvasculature within the heart may then cause loss of blood supply and be a factor in the
268 subsequent death of cardiomyocytes independent of direct viral replication.
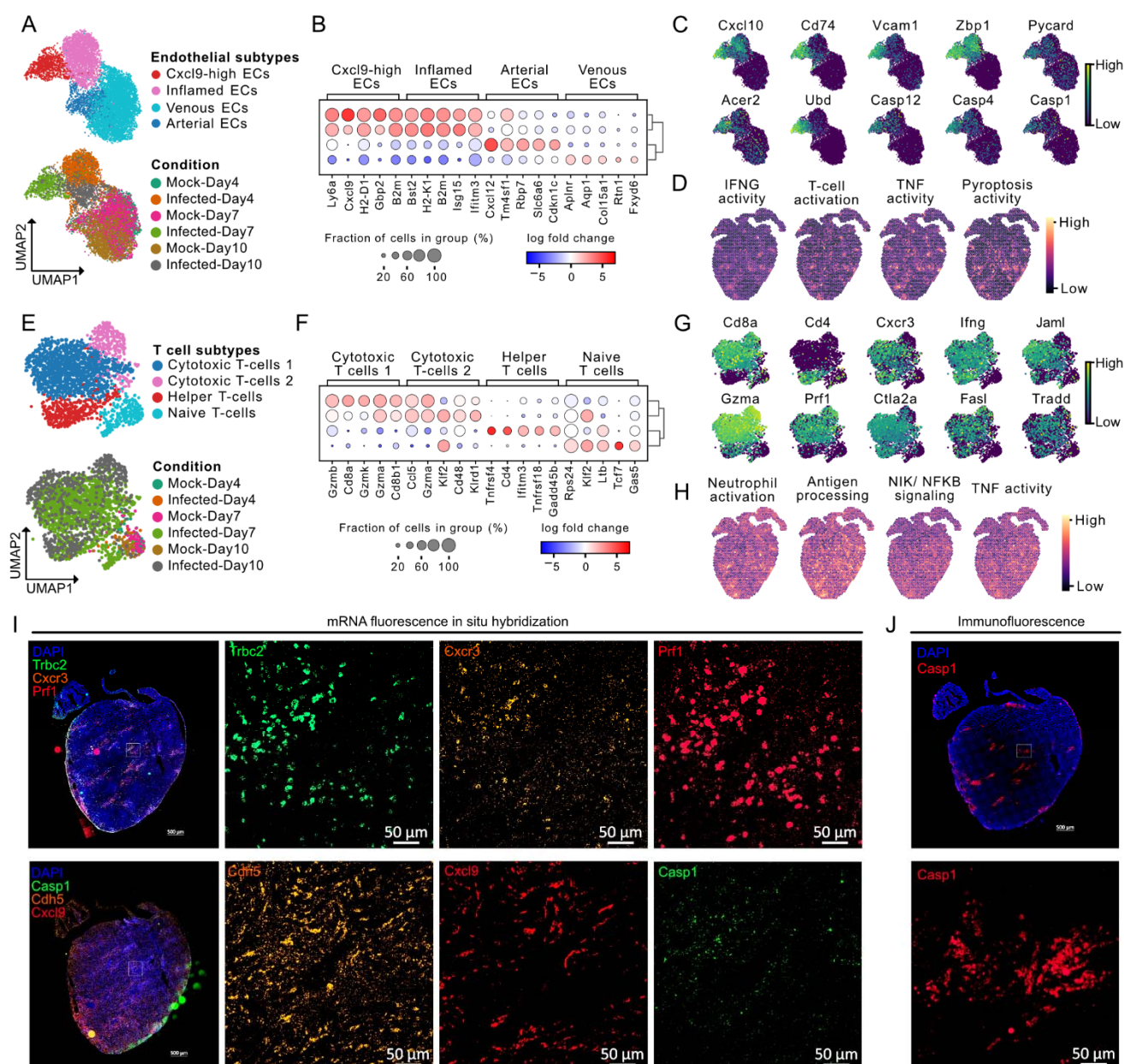
Figure 3: Cytotoxic T cells recruited by inflamed endothelial cells induce pyroptosis in myocarditic tissue A) UMAP plot of 9,786 single-cell endothelial cell transcriptomes from mock-infected and reovirus-infected hearts at 4, 7, and 10 dpi colored by endothelial cell (EC) subtype clusters (phenotypes) (top) and condition (bottom). **B)** Heatmap showing top-five differentially expressed genes (two-sided Wilcoxon test, log fold-change > 1.0 and p-value < 0.01) for endothelial cell subtypes. **C)** UMAP plot showing the expression of genes upregulated in *Cxcl9*-high endothelial cells. **D)** Spatial transcriptomic maps of cardiac tissue from reovirus infected hearts at 7 dpi showing gene module scores calculated for four GO terms enriched in *Cxcl9*-high endothelial cells. **E)** UMAP plot of 2,205 single-cell T cell (TC) transcriptomes from mock-infected and reovirus-infected hearts at 4, 7, and 10 dpi colored by T cell subtype clusters (top) and condition (bottom). **F)** Heatmap showing top-five differentially expressed genes (two-sided Wilcoxon test, log fold-change > 1.0 and p-value < 0.01) for T cell subtypes. **G)** UMAP plot showing the expression of genes upregulated in cytotoxic T cells from myocarditic heart at 7 dpi. **H)** Spatial transcriptomics maps of cardiac tissue from reovirus infected hearts at 7 dpi showing gene module scores calculated for four GO terms enriched in cytotoxic T cells. **I)** RNA FISH of T cell marker *Trbc2*, chemokine

10

283 receptor *Cxcr3*, lytic molecule *Prf1*, endothelial marker *Cdh5*, chemokine *Cxcl9*, and cell death marker *Casp1* on
284 sister sections in a myocarditic heart. **J)** Immunofluorescence images of Caspase 1 protein in a myocarditic heart.

Spatially restricted gene expression in myocarditic tissue

286 The spatially restricted nature of myocarditis motivated us to explore the spatial heterogeneity
287 of gene expression in reovirus-infected hearts. Our initial clustering of the spatial
288 transcriptomic data revealed distinct transcriptional programs for myocarditic regions, the
289 tissue bordering these myocarditic regions, and the rest of the ventricular tissue (**Fig. 1C, 4A,**
290 **Supp Fig. 2A**). Differential spatial gene expression analysis for these regions revealed
291 upregulation in the myocarditic regions of cell-type markers for infiltrating immune cells, (*Cd8a*
292 and *Gzma* for T cells, *Nkg7* for NK cells, *S100a8* for neutrophils), markers of inflammation
293 (*Cd52* and *Lyc62,* **Supp Fig. 9A-B**), and chemokines and cytokines (*Ccl5*, *Ccl2, Cxcl9,* and
294 *Cxcl10*). Analysis of the corresponding scRNA-seq data showed that *Ccl5* is expressed by
295 dendritic cells, *Ccl2* by fibroblasts, and *Cxcl9* and *Cxcl10* by endothelial cells. The receptor for
296 *Ccl2*, *Ccr2*, is expressed in macrophages, indicating that fibroblasts use the *Ccl2-Ccr2* axis for
297 macrophage recruitment during myocardial inflammation, as described recently[20,21] (**Supp Fig.**
298 **9C**). Collectively these analyses suggest that chemokine-producing endothelial cells and
299 cytokine-producing fibroblast cells contribute to the recruitment of immune cells to the
300 myocarditic tissue.

301 Closer inspection of the myocarditic regions and border zones showed an upregulation of
302 additional genes of interest, including *Timp1*, *AW112010*, *Clu*, *Ankrd1*, *Gm4841, and Ctss*
303 (**Fig. 4B**). *Timp1* was mainly expressed by inflamed fibroblasts in the scRNA-seq data (**Supp**
304 **Fig. 9D**). *Timp1* is a natural inhibitor of the matrix metalloproteinases (MMPs), a group of
305 peptidases involved in the degradation of the extracellular matrix. Upregulation of *Timp1* in
306 patients with deteriorating heart failure was reported previously[22]. *AW112010* was expressed
307 by inflamed endothelial cells and fibroblasts in the scRNA-seq data. *AW112010* encodes an
308 interferon-induced small secreted protein with a crucial role in the innate immune response to
309 infection and inflammation[23] (**Supp Fig. 9D**). *Clu* was expressed in a subset of inflamed cells
310 from all cardiac cell types in our data. *Clu* was shown to be upregulated during severe
311 myocarditis[24] (**Supp Fig. 9D**). *Ctss* was expressed mainly in monocytes (**Supp Fig. 9D**). *Ctss*
312 encodes a protease used for degradation of antigenic proteins to peptides for presentation by
313 MHC class II molecules. Increased formation of immunoproteasomes in susceptible mice has
314 been shown to affect the generation of antigenic peptides and subsequent T cell activity in viral
315 myocarditis[25,26]. GO term analysis of genes upregulated in the border zone revealed
316 enrichment of terms related to the response to tumor necrosis factor, response to interleukin-1,
317 and NIK/ NF-κB signaling (**Supp Fig. 9E**).

318 To further understand the effect of immune cell infiltration on the cell type composition
319 surrounding the myocarditic regions, we assessed cell type proportions as a function of
320 distance from myocarditic regions in the tissue. We quantified the cell type proportions in
321 myocarditic regions, the border zones, and the rest of the ventricular tissue, and found that the

322   fraction of *Cxcl9*-high endothelial cells, *Ccl2*+ fibroblasts, T cells, dendritic cells, and NK cells
323   was increased in the myocarditic regions, and the fraction of cardiomyocytes was reduced in
324   myocarditic regions (**Fig. 4C**, **Supp Fig. 2C**).

325   To understand the phenotype of *Ccl2*+ fibroblasts enriched in myocarditic region and border
326   zone, we reclustered 9,192 fibroblast cells from the scRNA-seq dataset and identified a distinct
327   cluster of inflamed *Ccl2*+ fibroblasts from the infected heart at 7 dpi (**Supp. Fig. 9F, 9G**). The
328   *Ccl2*+ fibroblasts expressed high levels of MHC class 1 (*H2-D1* and *H2-K1*), adhesion marker
329   genes *Vcam1* and *Icam1*, and other genes such as *Serpina3g*, *C3*, and *Ms4a4d* (**Supp Fig.**
330   **9H, 9I**). Moreover, these cells also expressed *Casp1* and *Casp4*, suggesting that fibroblasts
331   also undergo pyroptosis in response to cytotoxic T cells (**Supp Fig. 9H**).

332   To investigate the effect of inflammation on cardiomyocytes in myocarditic hearts, we
333   reclustered 502 cardiomyocytes from the scRNA-seq dataset and identified three distinct
334   phenotypes: ***i)*** ventricular myocytes expressing *Myl2*, *Myl3*, and *Mb* derived from mock and
335   infected hearts at 4 and 10 dpi, ***ii)*** atrial myocytes expressing markers *Myl4*, *Myl7*, and *Nppa*
336   derived from mock and infected hearts at 4 and 10 dpi, and ***iii)*** inflamed myocytes from the
337   infected heart at 7 dpi expressing innate immunity genes *Isg15*, *Igtp*, and *Iigp1*[27] (**Fig. 4D-E**).
338   Inflamed myocytes from the infected heart at 7 dpi had a distinct phenotype when compared to
339   the myocytes from hearts at 4 and 10 dpi, which clustered with myocyte cells from mock-
340   infected hearts (**Fig. 4E**). To find transcriptional signatures for myocytes present in the border
341   zone, we selected genes that were both enriched in cardiomyocytes in the scRNA-seq data
342   and upregulated in the border zone. This analysis revealed that cardiomyocytes in the border
343   zone expressed *Gm4841*, *Gm12185*, *Mt1*, *Mt2*, *Ankrd1*, and *Nppb* (**Fig. 4F, Supp Fig. 9J**).
344   *Gm4841* and *Gm12185* are interferon-inducible genes produced in response to interferon-
345   gamma. *Mt1* and *Mt2* genes modulate inflammation and support remodeling in ischemic
346   cardiomyopathy in mice[28]. Upregulation of *Ankrd1*, a myocyte survival factor, occurs during
347   late-stage heart disease in patients with idiopathic dilated cardiomyopathy[29]. A recent study
348   shows that cardiomyocytes expressing *Ankrd1* are localized in the border zone on day 1 post-
349   myocardial infarction[30]. Together, our analysis reveals that tissue injury is localized to
350   myocarditic regions with remodeling programs being active in the border zone and
351   demonstrates the importance of spatially resolved molecular measurements to study viral
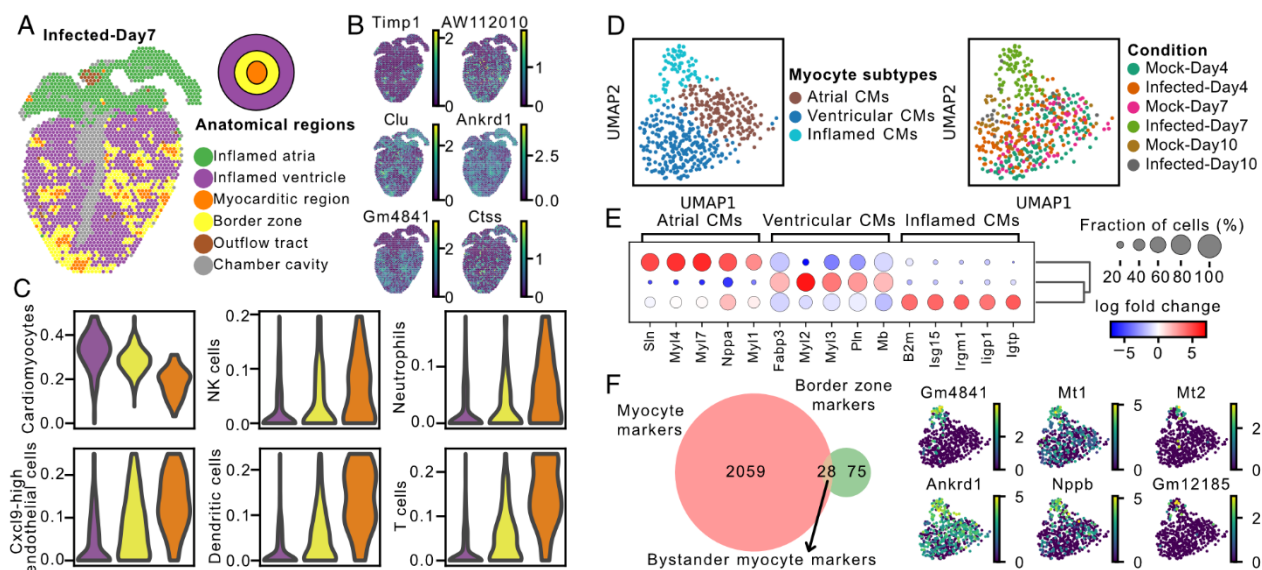352   myocarditis.

Figure 4: Myocarditic regions and the border zone have distinct transcriptomic profiles and cell type specific signatures. A) Spatial transcriptomics map of cardiac tissue section from reovirus-infected mice at 7 dpi colored by spot clusters representing transcriptionally distinct tissue regions. **B)** Spatial transcriptomics maps of cardiac tissue sections from reovirus-infected mice at 7 dpi showing the expression of differentially expressed genes of interest in the myocarditic and the border zone. **C)** Changes in average predicted cell-type proportions across the infected ventricle, for cell types enriched in the myocarditic region and the border zone. **D)** UMAP plot of 502 single-cell cardiomyocyte cell transcriptomes from mock-infected and reovirus-infected hearts at 4, 7, and 10 dpi colored by myocyte cell subtype (phenotypes) (left) and condition (right). **E)** Heatmap showing top-five differentially expressed genes (two-sided Wilcoxon test, log fold-change > 1.0 and p-value < 0.01) for cardiomyocyte cell subtypes. **F)** Venn Diagram showing myocyte-specific genes upregulated in the border zone around the myocarditic regions (left). UMAP plot showing the expression of myocyte-specific genes which are upregulated in the border zone of myocarditic regions (right).

Reduced adaptive immune cell infiltration associated with reovirus K287T mutant

We recently reported a reovirus mutant T1L S4-K287T (K287T) which has a point mutation in the S4 gene encoding outer capsid protein sigma-3 (σ3), a double-stranded (ds) RNA-binding multifunctional protein that promotes viral protein synthesis and facilitates viral entry and assembly[9]. This mutation abolishes the capacity of σ3 to block dsRNA-mediated activation of protein kinase R (PKR). The T1L K287T mutant is less virulent than the WT strain in neonatal mice. K287T replicates to WT titers in the heart at 4 dpi, but to significantly lower viral titers than WT virus at 7 dpi. The K287T mutant does not induce myocarditis as observed by calcium staining in the tissue[9]. To confirm our findings about immune-mediated pathogenesis during reovirus infection, we performed additional scRNA-seq for K287T infected hearts at 4, 7, and 10 dpi. We generated a total of 16,771 single-cell transcriptomes and integrated the data with the data from the WT virus. We did not observe sample-specific clusters after data integration, suggesting minimal experimental batch effects (**Fig. 5A, Supp Fig. 10A**). We performed viral transcript enrichment and compared the mean viral transcripts in WT- and mutant-infected cells. We found similar levels of mean viral transcripts for WT and K287T viruses at 4 dpi but a 60-fold lower viral load for K287T at 7 dpi, consistent with viral titer assays[9] (**Supp Fig. 10B, 10C**). We then compared the early cardiac cell type host responses to K287T and WT

13

infection. K287T induced a similar level of innate immune responses as WT virus with endothelial cells showing the highest increase in cardiac IR score (as defined before) at 4 dpi (**Fig. 5B**).

We analyzed the cell type composition of inflamed *Cxcl9*-high endothelial cells and immune cells detected in K287T- and WT-infected hearts. We observed fewer *Cxcl9*-high endothelial cells and immune cells including cytotoxic T cells, infiltrating the heart at 7 dpi compared to WT-infected heart (**Fig. 5C & 5F**). These differences correlate with the reduced levels of inflammation associated with the K287T mutant **(Supp Fig. 11A & 11B).** To validate these observations, we performed RNA FISH and immunofluorescence staining on K287T-infected hearts and compared them to mock-infected and reovirus WT-infected hearts (**Supp Fig. 11A**). Immunostaining for reoviral antigen in tissue sections confirmed both a significantly reduced area with viral replication (two-sided Mann-Whitney test, p-value < 0.05) and significantly lower viral antigen within those areas (two-sided Mann-Whitney test, p-value < 0.05), consistent with the scRNA-seq analysis and viral titer assays (**Supp. Fig. 11C, Fig. 5E**). We observed a reduction in infiltration of T cells in K287T-infected hearts as compared to WT-infected hearts at 7 dpi (**Fig. 5D, 5F**). The fraction of total cytotoxic immune cells (*Prf1*+) was significantly reduced in K287T-infected hearts as compared to WT-infected hearts (two-sided Mann-Whitney test, p-value < 0.05, **Supp. Fig. 11D**, **Fig 5F**). These findings support the reduced immune-mediated cytotoxicity seen in K287T-infected hearts. This was further supported by a significant reduction in Casp1 protein expression in K287T-infected hearts as compared to WT-infected hearts (two-sided Mann-Whitney test, p-value < 0.05, **Supp. Fig. 11C, Fig. 5G**). Our results show that cardiac endothelial cells mount a potent and robust innate immune response when infected with the K287T mutant virus. Clearance of the K287T virus from most infected cells by 7 dpi leads to a lower immune-mediated cytotoxicity, which correlates with lack of cardiac injury. These results suggest that a robust early innate immune response in endothelial cells is critical for early viral clearance and prevention of subsequent cardiac injury mediated by cytotoxic immune cells during reovirus-induced myocarditis.
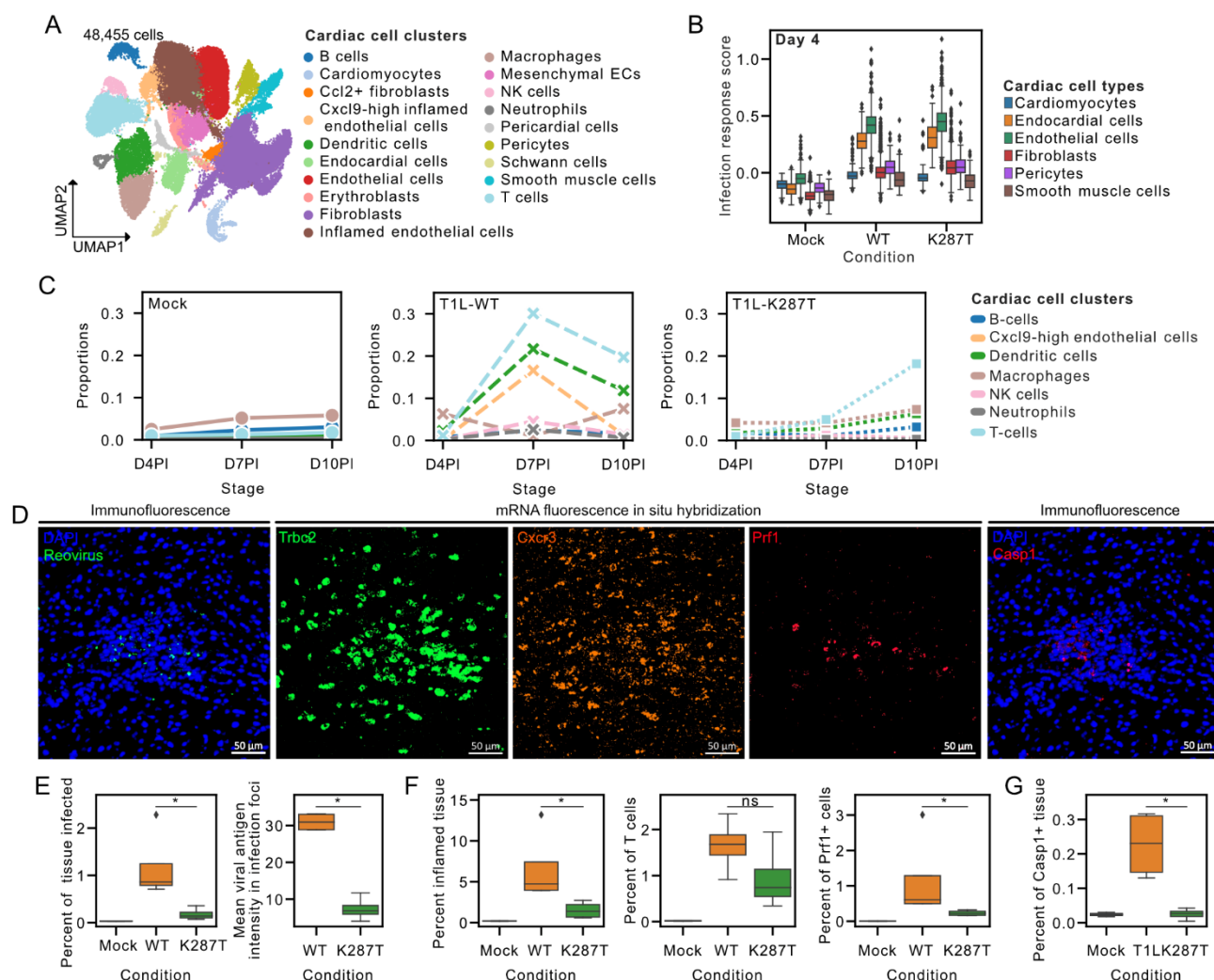
Figure 5: A robust innate immune response but reduced adaptive immune cell infiltration explains the non-myocarditic phenotype on infection with reovirus K287T mutant. A) UMAP plot of 48,455 single-cell cell transcriptomes from mock-infected, reovirus-wildtype (WT) infected, and reovirus mutant (K287T) infected hearts at 4, 7, and 10 dpi colored by cell-type clusters. **B)** Infection response score for cardiac cell types in scRNA-seq data across mock-infected, reovirus-WT infected, and reovirus-K287T infected hearts on 4 dpi. The infection response score represents the gene module score for a panel of 226 genes that are significantly upregulated in the reovirus-WT infected sample as compared to the mock-infected sample at 4 dpi. **C)** Changes in cell-type proportions with time for cell types detected in the myocarditic regions. Panels show the changes in cell-type proportions across mock-infected, reovirus-WT infected, and reovirus-K287T infected cells. **D)** Immunofluorescence images of reovirus antigen (left), RNA FISH images of T cell marker *Trbc2*, chemokine receptor *Cxcr3*, and lytic molecule *Prf1* (middle), and immunofluorescence images of Caspase1 protein (right) at 7 dpi. Full heart images included in the supplement material. **E-G)** Histology, RNA FISH, and immunofluorescence-based quantification of viral titers, T cells, and cytotoxicity. **E)** Percent of tissue area with viral antigen (left) and mean intensity of viral antigen inside myocarditic regions (right). **F)** Percent tissue inflammation (Hematoxylin & Eosin), percent T cells (*Trbc1+*, mRNA), and percent cytotoxic cells (*Prf1+*, mRNA). **G)** Percent of tissue area with Casp1 protein expression. **E-G)** Two-sided Mann-Whitney-Wilcoxon statistical test was used for comparison of data points between WT and K287T conditions. * represents p-value between 0.01 and 0.05.

15

DISCUSSION

Viral myocarditis has been recognized as a cause of heart failure for more than 50 years, but it is still a challenging disease to study, diagnose, and treat[31]. Here, we used integrated spatial and single-cell RNA-seq to dissect the temporal, spatial, and cellular heterogeneity of reovirus-induced acute myocarditis in a neonatal mouse model. We assayed ileum and heart tissues at multiple time points after infection. We investigated the cell types that are infected, and the cellular and spatial heterogeneity of innate and adaptive immune responses. We generated a total of thirteen scRNA-seq and eight spatial transcriptomics datasets, spanning two organs, four time points, and three infection conditions. Our data provide detailed insight into the chronology of molecular events that lead to reovirus-induced myocarditis. After oral inoculation, reovirus T1L infects entero-endocrine and enterocyte cells in the gut epithelium within 1 dpi. These cells mount a potent innate immune response to inhibit viral replication. The virus then infects the gut lymphatic cells within 4 dpi and is transmitted via lymphatics to the bloodstream and then to secondary sites in the body, including the heart. Around 4 dpi, the virus infects the endothelial cells lining the cardiac vasculature. Endothelial cells mount a potent innate immune response in the heart. In symptomatic cases, inflamed endothelial cells secrete chemokines that recruit circulating immune cells, including cytotoxic T cells. Tissue-infiltrating cytotoxic T cells then induce pyroptosis in the infected tissue inducing myocarditis. Overall, our experiments reveal a dynamic and spatially heterogeneous network of cellular phenotypes and cell-cell interactions associated with reovirus-induced myocarditis.

Integrated high-throughput scRNA-seq and spatial transcriptomics was recently used to study heart development[32,33] and heart disease[30,34], but these methods have not been used to study viral myocarditis prior to our work. Bulk RNA-seq has been used previously to profile transcriptomic signatures of infection, inflammation, and tissue injury associated with viral myocarditis[9,35–38]. Yet, these ensemble-level approaches do not capture the cellular and spatial heterogeneity of host response to infection. scRNA-seq has recently been used to study Coxsackievirus B3 (CVB3)-induced myocarditis in a mouse model[39]. Lasrado et al. report inflammatory phenotypes of myeloid cells, the role of fibroblasts in remodeling and inflammation, and the role of cytotoxic T-cells in CVB3-induced myocarditis. However, the cardiac cell types that are targeted by the virus, the cell type heterogeneity in basal interferon response and innate immune response, and the spatial restriction of transcriptional programs were not explored in this study.

Reovirus infection occurs often in humans, but most cases are mild or subclinical. These viruses display a broad host range, but only young hosts develop the disease. After infection of neonatal mice, reoviruses cause injury to a variety of organs, including the heart, liver, and the central nervous system, depending on the viral strain. Reovirus Type-1-Lang (T1L) strain is mildly virulent and causes myocarditis in ~50% of the infected mice. Neonatal mice with myocarditic hearts due to T1L infection survive with tissue damage and have an increased rate of heart failure. Therefore, reovirus T1L infection in neonatal mice is an ideal model to study the mechanisms and pathogenesis of reovirus induced myocarditis in young hosts. Previous

16

469 studies have claimed that the direct cytopathic effect of viral replication on cardiac cells is the
470 main cause of cardiac damage during reovirus-induced myocarditis[7,40]. Notably, Sherry et al.
471 found that reovirus infection can induce myocarditis in immunodeficient mice lacking B and/or
472 T cells, suggesting that reovirus-induced myocarditis does not strictly require adaptive
473 immunity[7,11]. However, these previous experiments do not rule out the possibility that the host
474 adaptive immune response can augment or delimit the nature and amount of host damage in
475 immune-competent mice, as is suggested by our work. Holm et al. and Stewart et al. have
476 studied the protective role of innate immune responses in reovirus-induced myocarditis[13,41].
477 However, prior to this study the temporal, spatial, and cell type heterogeneity of basal type-I
478 IFN and innate immune responses to infection had not been characterized. Miyamoto et al.
479 and Stewart et al. compared basal levels of type-I IFN between cardiac myocytes and
480 fibroblasts *in vitro* but these studies did not include all the cell types that make up complex
481 cardiac tissues[27,42].

482 Spatiotemporal characterization of viral myocarditis is crucial to understanding the viral and
483 host factors that are important for disease pathology. This knowledge may ultimately lead to
484 novel diagnostic approaches and better treatments. Several viruses that frequently infect
485 humans can cause myocarditis, including Adenovirus, enteroviruses, Epstein-Barr virus,
486 human Herpesvirus 6, parvovirus B19, and SARS-CoV2. The results presented here may not
487 be representative of the mechanisms for other viral causes of myocarditis or viral myocarditis
488 in adult hosts. However, the approaches that we have implemented here can be used in future
489 studies to investigate how the induction, pathophysiology, and course of myocarditis induced
490 by these viruses differs. We hope that the data and analysis routines that we make available
491 here will be a valuable resource for such future studies.

492 **METHODS**

493 **Reovirus infections of neonatal C57BL/6J mice.**

494 Confirmed pregnant female C57BL/6J mice were ordered from Jackson Laboratories to be
495 delivered at embryonic stage E14.5. Litters weighing 3 gram/ pup were gavaged using
496 intramedic tubing (Becton Dickinson 427401) per os with 50 μl with 10^7 PFU reovirus type 1
497 lang (T1L): wildtype or K287T mutant in 1x phosphate buffered saline (PBS) containing green
498 food color (McCormick) via a 1ml tuberculin slip tip syringe (BD 309659) and 30G x 1/2 needle
499 (BD 305106). Litters treated with 1x PBS containing green food color alone on the same day
500 were used as mock controls for the respective infection groups. The mock-infected and
501 reovirus-infected mice pups were weighed daily until the time points used in the study (days 1,
502 4, 7, and 10). Due to the difficulty in determining the sex of mice during infection and early
503 neonatal stages, we randomly selected the mice to collect ileum and heart tissues for
504 scRNAseq and spatial transcriptomics. All animal work was conducted ethically, conforming to
505 the U.S. Public Health Service policy, and was approved by the Institutional Animal Care and
506 Use Committee at Cornell University (IACUC Number 2019-0129).

Sample preparation for single-cell transcriptomics of cardiac tissue.

We sacrificed mock-infected and reovirus-infected C57BL/6J mice on day 4, day 7, and day 10 post-infection and collected cardiac tissues for single cell transcriptomics. Single heart tissue from respective stages (one heart per stage) were isolated aseptically, washed with ice-cold Hank's Balanced Salt Solution, HBSS (with calcium and magnesium chloride; Gibco 14025-134), and minced into 1-2mm pieces. Cardiac tissue pieces were then digested in tissue dissociation media with 200U/mL collagenase type II (Gibco 17100-015), 1 mg/ml dispase (Sigma D4693), and 3mM calcium chloride in HBSS for four cycles of 10 minutes under mild agitation at 37°C in 1.5 ml eppendorf tubes. After every 10-minute cycle, cell suspension was collected, added to ice-cold 1x PBS with 0.04% bovine serum albumin (BSA; Sigma A3803) and new dissociation media was added to the tubes. At the end of the digestion, the cells were passed through a 70µm filter and centrifuged into a pellet. To remove most blood contaminants, samples were resuspended in an ammonium-chloride-potassium (ACK) lysis buffer (Lonza #10-548E) for 3-5 minutes and centrifuged. Samples were then washed again in PBS with 0.04% BSA and then resuspended at 1×10^6 cells per ml. Cells from each sample were stained with Trypan Blue and cell viability was calculated on an automated cell counter (Countess II) before loading the cells on 10x Chromium. We used these cell viabilities to adjust the number of cells loaded on 10x Chromium to get the desired number of transcriptomes from viable cells for each sample (5000 cells per sample).

Sample preparation for single-cell transcriptomics of intestinal tissue.

We sacrificed mock-infected and reovirus-infected C57BL/6J mice on days 1 and 4 post-infection and collected intestinal ileum tissue for single cell transcriptomics. Single intestinal ileum tissue from respective stages (one tissue per stage) were isolated aseptically, washed with ice-cold Hank's Balanced Salt Solution, HBSS (without calcium and magnesium chloride; Gibco 14175-095) to remove contamination. The ileum tissue was then opened longitudinally, washed again with HBSS, and minced into 1-2mm pieces. To isolate the epithelial layer of cells, ileum tissue pieces were incubated in HBSS with 10mM Ethylenediaminetetraacetic acid (EDTA, Invitrogen 15575-038) and 1mM Dithiothreitol, (DTT, Sigma 43816-10ML) for two cycles of 10 minutes under mild agitation at 37°C. After every 10-minute cycle, cell suspension containing the intestinal epithelial cells was collected, added to ice-cold 1x PBS with 0.04% bovine serum albumin (BSA; Sigma A3803). The undigested pieces of lamina propria were then washed thoroughly with PBS (with calcium and magnesium chloride; Gibco 14080-055) to get rid of all EDTA. These pieces were then transferred to fresh tubes and incubated in 200U/ml Collagenase type I (Gibco 17100-017) and 3mM calcium chloride in PBS for three cycles of 10 minutes under mild agitation at 37°C in 1.5 ml eppendorf tubes. After every 10-minute cycle, cell suspension containing the lamina propria cells was collected, added to ice-cold phosphate buffered saline, PBS with 0.04% BSA in separate tubes. At the end of the digestion, the cells were passed through a 40µm filter and washed twice in PBS with 0.04% BSA and then resuspended at 1×10^6 cells per ml. Cells from intestinal epithelium and lamina propria for each sample were stained with Trypan Blue and cell viability was calculated

18

547 on automated cell counters (Countess II). Cell counts adjusted with viability were then pooled
548 as 40% epithelial cells and 60% lamina propria to adjust the number of cells loaded on 10x
549 Chromium and to get the desired number of transcriptomes from viable cells for each sample
550 (5000 cells per sample).

Single-cell RNA sequencing library preparation.

551

552 5000-6000 viable cells per sample (for heart and ileum tissues) were targeted on the
553 Chromium platform (10x Genomics) using one lane per sample per time point. Single-cell
554 libraries were built using the Chromium Next GEM Single Cell 3' Library Construction V3 Kit
555 (10x Genomics) and were then sequenced on an Illumina NextSeq 500 using 75 cycle high
556 output kits (Index 1 = 8, Read 1 = 28, and Read 2□=□55) for all samples. Sequencing data
557 were aligned to a combined mouse and reovirus reference genome (described below) using
558 the Cell Ranger 6.0.0 pipeline (10x Genomics).

Sample preparation for Visium spatial transcriptomics.

559

560 Whole hearts and intestinal ileum were isolated using aseptic techniques and placed in ice
561 cold sterile Hank's Balanced Salt Solution, HBSS (without calcium and magnesium chloride;
562 Gibco 14175-095). Blood and other contamination were carefully removed by perfusing the
563 tissues with fresh HBSS. Fresh tissues were immediately embedded in Optimal Cutting
564 Compound (OCT) media (SAKURA 25608-930) and frozen in a liquid-nitrogen-cooled
565 isopentane (EMD Millipore, MX0760) bath for spatial transcriptomics experiments. The tissue
566 blocks were cut into 10μm sections using Thermo Scientific CryoStar NX50 cryostat and
567 mounted on Visium Gene Expression slides (10x Genomics), which were pre-cooled to -20°C
568 and used for the Visium Spatial Gene Expression experiment.

Visium spatial transcriptomics library preparation.

569

570 We used the Visium Spatial Gene Expression (10x Genomics) platform for the spatial
571 transcriptomics experiments. Tissue sections from fresh-frozen hearts (mock-infected and
572 reovirus-infected at day 4 and day 7 post infection) and ileum (mock infected and reovirus
573 infected at day 1 and day 4 post infection) were mounted with one section per capture area on
574 individual Visium Gene Expression slides. These sections are then fixed in pre-chilled
575 methanol for 30 minutes and then hematoxylin and eosin (H&E) stained and imaged, which is
576 later used by the 10x Genomics Space Ranger (version 1.0.0) software to detect the spots
577 which are covered by the tissue. The optimal permeabilization time for 10 μm thick sections
578 was found to be 18 minutes for the heart and 12 minutes for the ileum using the 10x Genomics
579 Visium Tissue Optimization kit. Spatially tagged cDNA libraries were built using the 10x
580 Genomics Visium Spatial Gene Expression 3' Library Construction V1 Kit. H&E-stained heart
581 tissue sections were imaged using Zeiss PALM MicroBeam laser capture microdissection
582 system at 20x objective and the images were stitched and processed using Fiji ImageJ
583 software. cDNA libraries were sequenced on an Illumina NextSeq 500/550 using 150 cycle

19

584 high output kits (Read 1□= 28, Read 2□=□120, Index 1□=□10, and Index 2□=□10) for ileum
585 and on an Illumina NextSeq 2K (P2 flow cell) using the 100-cycle kit (Read 1 = 28, Read 2 =
586 96, Index 1□=□10, and Index 2□=□10) for the heart samples. Fiducial frames around the
587 capture area on the Visium slide were aligned manually and spots covering the tissue were
588 selected using Loupe Browser 4.0.0 software (10x Genomics). Sequencing data was then
589 aligned to a combined mouse and reovirus reference genome (described below) using the
590 Space Ranger 1.0.0 (10x Genomics) pipeline to derive a feature spot-barcode expression
591 matrix. Visium slide number V19B23-046 was used for spatial transcriptomics experiment on
592 mice hearts (mock-infected 4 dpi: capture area D1, reovirus-infected 4 dpi: capture area B1,
593 mock-infected 7 dpi: capture area C1, and reovirus-infected 7 dpi: capture area A1). Visium
594 slide number V19B23-045 was used for spatial transcriptomics experiment on mice ileum
595 tissue (mock-infected 1 dpi: capture area D1, reovirus-infected 1 dpi: capture area B1, mock-
596 infected 4 dpi: capture area C1, and reovirus-infected 4 dpi: capture area A1).

597 **Hybridization-based enrichment of viral fragments**

598 We performed a hybridization-based enrichment of viral fragments on a part of scRNA-seq
599 libraries using xGen NGS target enrichment kit (IDT; 1080577). In this approach, a panel of 5'-
600 biotinylated oligonucleotides is used for capture and pulldown of target molecules of interest,
601 which are then PCR amplified and sequenced. We designed a panel of 202 biotinylated probes
602 tiled across the entire reovirus T1L genome to selectively sequence viral molecules from the
603 scRNA-seq libraries **(Supp Data 2)**. 300ng of fragmented and indexed scRNA-seq libraries
604 from reovirus-WT infected hearts, reovirus-mutant infected hearts, and reovirus-infected ileum
605 were pooled in three separate reactions for xGen hybridization capture. Two rounds of
606 hybridization capture using the xGen enrichment protocol were performed for every reaction to
607 enrich viral transcripts. Amplification was performed for a total of 18 PCR cycles after the first
608 round of capture. 50% of the amplified product was used for the second round of hybridization
609 capture and amplification was performed for a total of 5 PCR cycles after the second round of
610 enrichment. Post-enrichment products were pooled and sequenced on Illumina Mini-seq for
611 ileum libraries and NextSeq 500 for heart libraries.

612 **Reference genome and annotation**

613 *Mus musculus* genome and gene annotations (assembly: GRCm38) were downloaded from
614 the Ensembl genome browser, and reovirus strain Type-1-Lang genome and gene annotations
615 were downloaded and compiled from the NCBI browser. We have shared reovirus genome
616 sequence   and   annotation   files   on   figshare   with   the   identifier
617 https://doi.org/10.6084/m9.figshare.c.5726372. Genomes were processed using the Cell
618 Ranger v-3.0.0 (10x Genomics) pipeline's mkref command.

619 **Single-cell RNAseq data processing and visualization**

620   Cells with fewer than 200 unique genes or more than 25 percent of transcripts aligning to
621   mitochondrial genes were removed. After quality control, we captured 6596, 7096, and 3483
622   single-cell transcriptomes from mock-infected hearts, 5970, 5086, and 3453 single cell
623   transcriptomes from reovirus wild-type (WT)-infected hearts, and 5354, 7462, and 3955 cells
624   from reovirus mutant K287T-infected hearts at 4, 7, and 10 dpi respectively. The single-cell
625   transcriptomes were log-transformed and normalized using the Scanpy package verison-
626   1.8.1[43]. We used Scanpy to choose the highly variable genes with min_disp=0.5 and
627   max_mean=3 thresholds. We then performed mean centering and scaling while regressing out
628   total UMI counts, percent mitochondrial transcripts, S score, and G2M score, followed by
629   principal component analysis (PCA) to reduce the dimensions of the data to the top 20
630   principal components (PCs). Uniform Manifold Approximation and Projection (UMAP) and the
631   Nearest Neighbor (NN) graph were initialized in this PCA space using the first 20 PCs. The
632   cells were then clustered using the Leiden method with multiple values of clustering resolution
633   to get fine (resolution=0.5) and broad (resolution=0.3) celltype clusters. Cell-type-specific
634   canonical gene markers along with differentially expressed genes (wilcoxon method) for each
635   cluster were used to assign cell type labels. Normalized gene expression was visualized on
636   DotPlots, UMAP plots, and Violin plots across cell type groups. A few cell type clusters
637   representing cell states of the same cell type were grouped into broad cell type groups using
638   cell type marker genes and then used for downstream analysis. Differential gene expression
639   analysis (DGEA) was performed using the rank_gene_groups function in Scanpy with the
640   Wilcoxon statistical method. All gene module scores were calculated using the score_genes
641   function in scanpy.

642   **Reclustering and analysis of endothelial cells, T cells, fibroblasts, and cardiomyocytes**

643   Normalized gene expression for a specific cell type group was extracted from the combined
644   scRNA-seq dataset. We used Scanpy to reselect the highly variable genes within that cell type
645   group with min_disp=0.5 and max_mean=3 thresholds. We then performed mean centering
646   and scaling while regressing out total UMI counts, percent mitochondrial transcripts, S score,
647   and G2M score, followed by principal component analysis (PCA) to reduce the dimensions of
648   the data to the top 20 principal components (PCs). Uniform Manifold Approximation and
649   Projection (UMAP) and the Nearest Neighbor (NN) graph were initialized in this PCA space
650   using the first 20 PCs. The cells were then reclustered using the Leiden method
651   (resolution=0.5 for endothelial cells, resolution=0.3 for T cells, resolution=0.2 for fibroblasts,
652   and resolution=0.3 for cardiomyocytes) to get cell type subclusters. Differentially expressed
653   genes (wilcoxon method) for each subcluster were then used to assign cell subtype labels.
654   Subclusters representing doublets and expressing markers of multiple cell types were then
655   removed from the analysis. Normalized gene expression for differentially expressed genes and
656   genes of interest was visualized on DotPlots and UMAP plots across celltype subgroups.
657   Differential gene expression analysis (DGEA) was performed using the rank_gene_groups
658   function in Scanpy with the Wilcoxon statistical method. All gene module scores were
659   calculated using the score_genes function in Scanpy.

Spatial transcriptomics data processing, integration, analysis, and visualization

Spatial transcriptomics data from barcoded spatial spots from four heart sections were log-normalized using the Scanpy package (v1.8.1). Scanpy package was then used to select highly variable genes for spatial transcriptomics data with min_disp=0.5 and max_mean=3 thresholds. We then performed mean centering and scaling while regressing out total UMI counts, percent mitochondrial UMIs, S score, and G2M score, followed by PCA on the spot gene expression matrix, and reduced the dimensions of the data to the top 20 principal components. UMAP and the NN graph were initialized in this PCA space. The spots were then clustered using the Leiden method with multiple values of clustering resolution. The method returned spot clusters representing different tissue regions, which were then visualized on H&E images as spatial transcriptomics maps for individual samples to assign anatomical regions. Normalized gene expression was visualized on spatial transcriptomics maps for all tissue sections. Spot clusters representing the same tissue regions were grouped into broad anatomical region groups using marker genes and then used for downstream analysis. Stereoscope deconvolution method implemented in the scvi-tools[44] (v0.12.2) package was used for integration of spatial transcriptomics data with time-matched scRNA-seq data and cell type prediction values for spatial transcriptomics spots were estimated for the infected heart at 7 dpi. DGEA for anatomical regions was performed using the rank_gene_groups function in Scanpy with the Wilcoxon statistical method.

Viral transcript sequencing data processing, filtering, and visualization

Enriched viral transcript data were aligned to a combined mouse and reovirus Type-1-Lang genome for all infected samples. Viral unique molecule (UMI) counts were taken from the combined expression matrices and added as metadata in the host gene expression data. Viral UMI counts in empty droplets, droplets with low-quality cells (< 200 host UMI counts), droplets with viable cells (>=200 host UMI counts) were sorted by viral UMI and visualized on a histogram to filter out the cell-free ambient viral RNA enriched in the hybridization protocol. Using the distribution of viral UMI counts in empty droplets, thresholds of two viral UMIs and five viral UMIs were used to identify infected cells in the heart and ileum respectively (**Supp Fig 2D**). Viral transcripts in the infected cells were then visualized on a DotPlot to determine viral tropism in tissues.

Gene Ontology term enrichment analysis for scRNA-seq and spatial transcriptomics

Gene Ontology (GO) term enrichment analysis was performed on differentially expressed genes using gseapy (v0.10.4) wrapper package[45]. Differentially expressed genes (two-sided Wilcoxon test, log fold-change threshold = 2.0, p-value < 10^{-4} for scRNA-seq cells, and log fold-change threshold = 0.5, p-value < 10^{-2} for spatial transcriptomics spots) were selected and used for GO term enrichment analysis using GO_Biological_Processes_2021 gene sets in enrichr command[46]. The enriched GO terms of interest were selected and visualized on a

697 BarPlot. The genes associated with GO terms of interested were used to calculate module
698 scores using score_genes command in Scanpy.

699 Sample preparation for RNA fluorescence in-situ hybridization (FISH),
700 immunofluorescence, and histology

701 Whole hearts were isolated using aseptic technique and placed in ice cold sterile Hank's
702 Balanced Salt Solution and then blood was carefully removed by perfusing the hearts with
703 fresh HBSS through the apex. Fresh tissues were immediately embedded in Optimal Cutting
704 Compound (OCT) media and frozen in liquid nitrogen cooled isopentane, cut into 10 μm
705 sections using a Thermo Scientific Microm 550 cryostat, and mounted on -20°C cooled
706 histological glass slides which were then stored at -80°C until used.

707 RNA fluorescence in-situ hybridization (FISH) split probe design and Signal
708 Amplification using Hybridization Chain Reaction HCR-V3

709 Two-step hybridization strategy with split probe design and Hybridization Chain Reaction
710 (HCR)-V3[47] was used to label up to three transcripts in a single tissue section. Probes were
711 designed using NCBI primer-blast which uses primer3 for designing internal hybridization oligo
712 and BLASTn to check for binding specificity. We designed 20-21 bp primer pairs for an
713 amplicon length of 40-42 bp (2 x primer length), primer melting temperature between 57°C and
714 63°C, and primer GC content between 35% and 65%. 7-10 sets of reverse complemented
715 forward primers and reverse primers were then concatenated to flanking initiator sequence for
716 HCR, ordered from Integrated DNA Technologies (IDT) with standard desalting purification
717 (**Supp Data 3**). Split probes for each gene target, mixed and diluted in nuclease-free water to
718 create a split probe pool stock solution at 10μM total probe concentration for every target.
719 Hairpin pairs labeled with three different fluorophores namely Alexa-488, Alexa-546, and
720 Alexa-647 (Molecular Instruments, **Supp Data 4**) were used for HCR V3.

721 RNA fluorescence in-situ hybridization (FISH) experiments

722 Slides with tissue sections were then brought to room temperature until the OCT melts and
723 were then immediately fixed in 4% paraformaldehyde for 12 minutes at room temperature.
724 Post fixation, the sections were washed for 5 mins in 1x PBS twice, incubated for 1 hour in
725 70% ethanol for tissue permeabilization, washed again for 5 mins in 1x PBS, and then used for
726 primary hybridization. Hybridization Buffer (HB) mix was prepared with 2x SSC, 5x of Denhart
727 Solution, 10% Ethylene Carbonate, 10% Dextran Sulfate, 0.01% SDS, 1uM of probe pool mix
728 per target for the hybridization reaction. 20 μl of HB mix (with probes) per section was then put
729 on each slide to cover the tissue section, covered with parafilm, and incubated overnight at
730 37°C inside a humidifying chamber for primary hybridization. After primary hybridization,
731 parafilm was removed and slides were washed in Hybridization Wash Buffer-1 (0.215M NaCl,
732 0.02M Tris HCl pH 7.5, and 0.005M EDTA) for 20-30 minutes at 48°C. Amplification Buffer
733 (AB) mix was prepared with 2x SSC, 5x of Denhart Solution, 10% Dextran Sulfate, 0.01%

734 SDS, 0.06µM of HCR hairpins for the amplification reaction. 2ul of each fluorophore labeled
735 hairpins at 3µM corresponding to the target genes were mixed, incubated at 95°C for 1.5
736 minutes, covered in aluminum foil, and left to cool down at room temperature for 30 minutes to
737 form hairpins before adding it to AB mix. 20 µl of AB mix per section was then put on each
738 slide to cover the tissue section, covered with parafilm, and incubated overnight at room
739 temperature in dark for signal amplification. After signal amplification, parafilm was removed,
740 and slides were washed in 5x SSCT buffer twice for 30-40 minutes and then twice for 10 mins.
741 The slides were then carefully cleaned with Kimwipe and treated with Ready Probes Auto-
742 fluorescence Quenching Reagent Mix (Thermo Fisher, R37630) for 5 minutes and washed
743 three times in 1X PBS. Last, tissue sections were then counter stained with DAPI for 10
744 minutes at room temperature, washed for 5 minutes in 1x PBS twice, excess PBS cleaned
745 using Kimwipe, immediately mounted on coverslips using Slowfade antifade media, left
746 overnight for treatment, and imaged the next day on a Zeiss Axio Observer Z1 Microscope
747 using a Hamamatsu ORCA Fusion Gen III Scientific CMOS camera. smFISH images were
748 shading corrected, stitched, rotated, thresholded, and exported as TIFF files using Zen 3.1
749 software (Blue edition).

750 **Immunofluorescence Assays**

751 Slides with tissue sections were brought from -80°C freezer and heated for 1 minute at 37°C
752 until the OCT melts and were then immediately dipped in prechilled methanol at -20°C for 30
753 minutes. After fixation, the slides were then rehydrated to Milli-Q water for 2 minutes and then
754 washed twice in 1X PBS. Samples then underwent an antigen retrieval step via incubation in
755 1X citrate buffer for 10-15 minutes at 95°C. Samples were then permeabilized in 0.1% Triton
756 X-100 in 1X PBS for fifteen minutes, washed three times in 0.05% Tween-20 in PBS (TBST),
757 blocked for one hour at room temperature in blocking buffer (1% bovine serum albumin and
758 10% normal donkey serum in PBS. 20ul of primary antibodies diluted in antibody solution (1%
759 bovine serum albumin in PBS) were then added on to the slides, covered with parafilm, then
760 incubated in a humidifying chamber overnight at 4°C. Primary antibodies used were rabbit anti-
761 reovirus VM1:VM6 polyclonal sera (1:30000), rat anti-Casp1 monoclonal antibody (1:200, #14-
762 9832-82, Invitrogen). After overnight primary incubation, samples were washed three times in
763 PBS and then incubated in secondary antibodies diluted in blocking solution for two hours at
764 room temperature. The secondary antibodies were donkey anti-rabbit alexa-488 (1:500, 711-
765 545-152, Jackson Immuno Research) and donkey anti-rat alexa-647 (1:500, ab150155,
766 Abcam). Lastly, samples were washed thrice in PBS for 10 minutes with shaking, counter
767 stained with DAPI, and mounted in Prolong antifade mounting media. Images were acquired
768 on a Zeiss Axio Observer Z1 Microscope using a Hamamatsu ORCA Fusion Gen III Scientific
769 CMOS camera. Immunostaining images were shading corrected, stitched, rotated,
770 thresholded, and exported as TIFF files using Zen 3.1 software (Blue edition).

771 **Processing and quantification of Histology, RNA FISH, and immunofluorescence**
772 **images**

773 Image analysis and processing for histology, immunofluorescence, and RNA FISH images was
774 done manually in Zen 3.1 software (Blue edition) and Fiji ImageJ. Whole heart Hematoxylin
775 and Eosin (H&E) images were thresholded using non-linear adjustments (gamma = 0.45)
776 applied across entire images using Zen 3.1 Blue software. For area quantifications from
777 Hematoxylin and Eosin (H&E) stained histology images, 3-color RGB images were opened in
778 ImageJ. The images were converted to greyscale 8-bit images and thresholded to detect the
779 entire tissue section area. Sites of inflammation were manually selected for calculating the
780 inflammation percentage in the tissue. For RNA FISH images, the images with DAPI
781 counterstain channel were manually thresholded to segment nuclei. Holes in nuclei
782 segmentation mask were files and morphological opening was performed to remove noise.
783 The segmentation was enhanced using watershed algorithm followed by a morphological
784 opening operation. For RNA FISH images, individual channels TIFF files exported from Zen
785 3.1 software were opened in ImageJ and converted to 8-bit images. Images were manually
786 thresholded using linear adjustments (gamma = 1.0) applied across entire images to detect
787 RNA-labelled cells and morphological opening was performed to remove noise. The nuclei and
788 cells were counted in all images using the Analyze Particle function in ImageJ. For
789 immunofluorescence images, individual channels were thresholded using linear adjustments
790 (gamma = 1.0) applied across entire images. Thresholded images were loaded in Fiji ImageJ
791 and converted to 8-bit images. The greyscale images for individual channels were then used to
792 segment signal using same thresholds across all tissue sections to get selections for area
793 quantifications. The tissue border was manually removed from the fluorescence channels
794 when calculating the area of interest. Entire hearts were manually selected using DAPI
795 channel to calculate total area of the tissue. Any changes to brightness and contrast were
796 applied equally across the entire image for visibility of fluorescence signal.

797 **ACKNOWLEDGEMENTS**

808 **AUTHOR CONTRIBUTIONS**

809 M.M., J.S.P., and I.D.V. designed the study. M.M., M.M.H., and S.T.C. performed the animal
810 experiments. M.M. and M.M.H. performed the scRNA-seq and spatial transcriptomics
811 experiments. M.M., D.W.M., and M.F.Z.W. analyzed the data. M.M. performed histology, RNA

25

812 FISH, and immunostaining experiments and analyzed the images. M.M., J.S.P., and I.D.V.
813 wrote the manuscript. All authors provided feedback and comments.

DATA AVAILABILITY

815 The authors declare that all sequencing data supporting the findings of this study have been
816 deposited in NCBI's Gene Expression Omnibus (GEO)[48] with GEO series accession number
817 GSE189636. Raw and processed H&E-stained tissue images and tissue-spot alignment files
818 matched to spatial transcriptomics datasets have been made publicly available on figshare
819 with identifier https://doi.org/10.6084/m9.figshare.c.5726372[49]. Scripts to reproduce the
820 analysis presented in this study have been deposited on GitHub
821 (https://github.com/madhavmantri/reovirus_induced_myocarditis).

CONFLICTS

823 The authors declare no conflicts.

REFERENCES

825 1. Pollack, A., Kontorovich, A. R., Fuster, V. & Dec, G. W. Viral myocarditis—diagnosis, treatment
826   options, and current controversies. *Nat. Rev. Cardiol. 2015 1211* **12**, 670–680 (2015).

827 2. Rose, N. R. Viral Myocarditis. *Curr. Opin. Rheumatol.* **28**, 383 (2016).

828 3. Yajima, T. & Knowlton, K. U. Viral myocarditis from the perspective of the virus. *Circulation* **119**,
829   2615–2624 (2009).

830 4. Tschöpe, C. *et al.* Myocarditis and inflammatory cardiomyopathy: current evidence and future
831   directions. *Nat. Rev. Cardiol.* **18**, 169–193 (2021).

832 5. Woodruff, J. F. Viral myocarditis. A review. *Am. J. Pathol.* **101**, 425 (1980).

833 6. Lasrado, N. & Reddy, J. An overview of the immune mechanisms of viral myocarditis. *Rev. Med.*
834   *Virol.* **30**, 1–14 (2020).

835 7. Sherry, B., Schoen, F. J., Wenske, E. & Fields, B. N. Derivation and characterization of an
836   efficiently myocarditic reovirus variant. *J. Virol.* **63**, 4840–4849 (1989).

837 8. Boehme, K. W., Lai, C. M. & Dermody, T. S. Mechanisms of reovirus bloodstream dissemination.
838   *Adv. Virus Res.* **87**, 1–35 (2013).

839 9. Guo, Y. *et al.* The multi-functional reovirus σ3 protein is a virulence factor that suppresses stress
840   granule formation and is associated with myocardial injury. *PLOS Pathog.* **17**, e1009494 (2021).

841 10. Swirski, F. K. & Nahrendorf, M. Cardioimmunology: the immune system in cardiac homeostasis
842   and disease. *Nat. Rev. Immunol. 2018 1812* **18**, 733–744 (2018).

843 11. Sherry, B., Li, X. Y., Tyler, K. L., Cullen, J. M. & Virgin, H. W. Lymphocytes protect against and
844   are not required for reovirus-induced myocarditis. *J. Virol.* **67**, 6119–6124 (1993).

845 12. Phillips, M. B., Dina Zita, M., Howells, M. A., Weinkopff, T. & Boehme, K. W. Lymphatic Type 1
846   Interferon Responses Are Critical for Control of Systemic Reovirus Dissemination. *J. Virol.* **95**,
847   (2021).

848 13. Holm, G. H. *et al.* Interferon Regulatory Factor 3 Attenuates Reovirus Myocarditis and
849   Contributes to Viral Clearance. *J. Virol.* (2010). doi:10.1128/jvi.01742-09

850 14. Schaum, N. *et al.* Single-cell transcriptomics of 20 mouse organs creates a Tabula Muris. *Nat.*
851   *2018 5627727* **562**, 367–372 (2018).

852 15. Kalucka, J. *et al.* Single-Cell Transcriptome Atlas of Murine Endothelial Cells. *Cell* **180**, 764-
853   779.e20 (2020).

854 16. Tokunaga, R. *et al.* CXCL9, CXCL10, CXCL11/CXCR3 axis for immune activation - a target for
855   novel cancer therapy. *Cancer Treat. Rev.* **63**, 40 (2018).

856 17. Woudstra, L., Juffermans, L. J. M., van Rossum, A. C., Niessen, H. W. M. & Krijnen, P. A. J.
857   Infectious myocarditis: the role of the cardiac vasculature. *Heart Fail. Rev.* **23**, 583–595 (2018).

858 18. Mai, J., Virtue, A., Shen, J., Wang, H. & Yang, X. F. An evolving new paradigm: endothelial cells
859   – conditional innate immune cells. *J. Hematol. Oncol. 2013 61* **6**, 1–13 (2013).

860 19. Chávez-Galán, L., Arenas-Del Angel, M. C., Zenteno, E., Chávez, R. & Lascurain, R. Cell death
861   mechanisms induced by cytotoxic lymphocytes. *Cell. Mol. Immunol.* **6**, 15–25 (2009).

862 20. Leuschner, F. *et al.* Silencing of CCR2 in myocarditis. *Eur. Heart J.* **36**, 1478–1488 (2015).

863 21. Miteva, K. *et al.* Mesenchymal Stromal Cells Modulate Monocytes Trafficking in Coxsackievirus
864   B3-Induced Myocarditis. *Stem Cells Transl. Med.* **6**, 1249–1261 (2017).

865 22. Barton, P. J. R. *et al.* Increased expression of extracellular matrix regulators TIMP1 and MMP1 in
866   deteriorating heart failure. *J. Heart Lung Transplant.* **22**, 738–744 (2003).

867 23. Jackson, R. *et al.* The translation of non-canonical open reading frames controls mucosal
868   immunity. *Nature* **564**, 434–438 (2018).

869 24. Swertfeger, D. K., Witte, D. P., Stuart, W. D., Rockman, H. A. & Harmony, J. A. K. Apolipoprotein
870   J/clusterin induction in myocarditis: A localized response gene to myocardial injury. *Am. J.*
871   *Pathol.* **148**, 1971–1983 (1996).

872 25. Szalay, G. *et al.* Ongoing Coxsackievirus Myocarditis Is Associated with Increased Formation
873   and Activity of Myocardial Immunoproteasomes. *Am. J. Pathol.* **168**, 1542–1552 (2006).

874 26. Van Der Borght, K. *et al.* Myocarditis elicits dendritic cell and monocyte infiltration in the heart
875   and self-antigen presentation by conventional type 2 dendritic cells. *Front. Immunol.* **9**, 2714
876   (2018).

877 27. Stewart, M. J., Smoak, K., Blum, M. A. & Sherry, B. Basal and Reovirus-Induced Beta Interferon
878   (IFN-β) and IFN-β-Stimulated Gene Expression Are Cell Type Specific in the Cardiac Protective
879   Response. *J. Virol.* **79**, 2979–2987 (2005).

880 28. Duerr, G. D. *et al.* Metallothioneins 1 and 2 Modulate Inflammation and Support Remodeling in
881   Ischemic Cardiomyopathy in Mice. *Mediators Inflamm.* **2016**, (2016).

882   29.   Bogomolovas, J. *et al.* Induction of Ankrd1 in dilated cardiomyopathy correlates with the heart
883   failure progression. *Biomed Res. Int.* **2015**, (2015).

884   30.   Yamada, S. *et al.* Spatiotemporal single-cell analysis reveals critical roles of mechano-sensing
885   genes at the border zone in remodeling after myocardial infarction. doi:10.21203/rs.3.rs-
886   620498/v1

887   31.   Gupta, S., Markham, D. W., Drazner, M. H. & Mammen, P. P. A. Fulminant myocarditis. *Nat.*
888   *Clin. Pract. Cardiovasc. Med. 2008 511* **5**, 693–706 (2008).

889   32.   Mantri, M. *et al.* Spatiotemporal single-cell RNA sequencing of developing chicken hearts
890   identifies interplay between cellular differentiation and morphogenesis. *Nat. Commun. 2021 121*
891   **12**, 1–13 (2021).

892   33.   Asp, M. *et al.* A Spatiotemporal Organ-Wide Gene Expression and Cell Atlas of the Developing
893   Human Heart. *Cell* **179**, 1647-1660.e19 (2019).

894   34.   Kuppe, C. *et al.* Spatial multi-omic map of human myocardial infarction. *bioRxiv*
895   2020.12.08.411686 (2020). doi:10.1101/2020.12.08.411686

896   35.   Lindner, D. *et al.* Association of Cardiac Infection With SARS-CoV-2 in Confirmed COVID-19
897   Autopsy Cases. *JAMA Cardiol.* **5**, 1281–1285 (2020).

898   36.   Bräuninger, H. *et al.* Cardiac SARS-CoV-2 infection is associated with pro-inflammatory
899   transcriptomic alterations within the heart. *Cardiovasc. Res.* (2021). doi:10.1093/CVR/CVAB322

900   37.   Onyimba, J. A. *et al.* The innate immune response to coxsackievirus B3 predicts progression to
901   cardiovascular disease and heart failure in male mice. *Biol. Sex Differ.* **2**, (2011).

902   38.   Coronado, M. J. *et al.* Testosterone and interleukin-1β increase cardiac remodeling during
903   coxsackievirus B3 myocarditis via serpin A 3n. *Am. J. Physiol. Heart Circ. Physiol.* **302**, (2012).

904   39.   Lasrado, N., Borcherding, N., Arumugam, R., Starr, T. K. & Reddy, J. Dissecting the Cellular
905   Landscape and Transcriptome Network in Viral Myocarditis by Single-Cell RNA Sequencing.
906   *bioRxiv* 2021.05.16.444367 (2021). doi:10.1101/2021.05.16.444367

907   40.   Baty, C. J. & Sherry, B. Cytopathogenic effect in cardiac myocytes but not in cardiac fibroblasts
908   is correlated with reovirus-induced acute myocarditis. *J. Virol.* **67**, 6295–6298 (1993).

909   41.   Stewart, M. J., Blum, M. A. & Sherry, B. PKR's protective role in viral myocarditis. *Virology* **314**,
910   92–100 (2003).

911   42.   Miyamoto, S. D. *et al.* Cardiac Cell-specific Apoptotic and Cytokine Responses to Reovirus
912   Infection: Determinants of Myocarditic Phenotype. *J. Card. Fail.* **15**, 529–539 (2009).

913   43.   Wolf, F. A., Angerer, P. & Theis, F. J. SCANPY: Large-scale single-cell gene expression data
914   analysis. *Genome Biol.* **19**, 1–5 (2018).

915   44.   Gayoso, A. *et al.* scvi-tools: a library for deep probabilistic analysis of single-cell omics data.
916   *bioRxiv* 2021.04.28.441833 (2021). doi:10.1101/2021.04.28.441833

917   45.   Subramanian, A. *et al.* Gene set enrichment analysis: A knowledge-based approach for
918   interpreting genome-wide expression profiles. *Proc. Natl. Acad. Sci.* **102**, 15545–15550 (2005).

919 46. Xie, Z. *et al.* Gene Set Knowledge Discovery with Enrichr. *Curr. Protoc.* **1**, e90 (2021).

920 47. Choi, H. M. T. *et al.* Third-generation in situ hybridization chain reaction: multiplexed,
921   quantitative, sensitive, versatile, robust. *Development* **145**, (2018).

922 48. Edgar, R. Gene Expression Omnibus: NCBI gene expression and hybridization array data
923   repository. *Nucleic Acids Res.* (2002). doi:10.1093/nar/30.1.207

924 49. Mantri, M. Reovirus-induced-myocarditis. (2021).
925   doi:https://doi.org/10.6084/m9.figshare.c.5726372